



MIT Open Access Articles

Ionization behavior of nanoporous polyamide membranes

The MIT Faculty has made this article openly available. **Please share** how this access benefits you. Your story matters.

As Published	10.1073/pnas.2008421117
Publisher	Proceedings of the National Academy of Sciences
Version	Final published version
Citable link	https://hdl.handle.net/1721.1/133409
Terms of Use	Article is made available in accordance with the publisher's policy and may be subject to US copyright law. Please refer to the publisher's site for terms of use.

Ionization behavior of nanoporous polyamide membranes

Cody L. Ritt^a, Jay R. Werber^a, Mengyi Wang^{b,c}, Zhongyue Yang^b, Yumeng Zhao^a, Heather J. Kulik^b, and Menachem Elimelech^{a,1}

^aDepartment of Chemical and Environmental Engineering, Yale University, New Haven, CT 06520; ^bDepartment of Chemical Engineering, Massachusetts Institute of Technology, Cambridge, MA 02139; and ^cDepartment of Materials Science and Engineering, Massachusetts Institute of Technology, Cambridge, MA 02139

Edited by Matthew V. Tirrell, The University of Chicago, Chicago, IL, and approved October 8, 2020 (received for review April 30, 2020)

Escalating global water scarcity necessitates high-performance desalination membranes, for which fundamental understanding of structure–property–performance relationships is required. In this study, we comprehensively assess the ionization behavior of nanoporous polyamide selective layers in state-of-the-art nanofiltration (NF) membranes. In these films, residual carboxylic acids and amines influence permeability and selectivity by imparting hydrophilicity and ionizable moieties that can exclude coions. We utilize layered interfacial polymerization to prepare physically and chemically similar selective layers of controlled thickness. We then demonstrate location-dependent ionization of carboxyl groups in NF polyamide films. Specifically, only surface carboxyl groups ionize under neutral pH, whereas interior carboxyl ionization requires pH >9. Conversely, amine ionization behaves invariably across the film. First-principles simulations reveal that the low permittivity of nanoconfined water drives the anomalous carboxyl ionization behavior. Furthermore, we report that interior carboxyl ionization could improve the water–salt permselectivity of NF membranes over fourfold, suggesting that interior charge density could be an important tool to enhance the selectivity of polyamide membranes. Our findings highlight the influence of nanoconfinement on membrane transport properties and provide enhanced fundamental understanding of ionization that could enable novel membrane design.

desalination | polyamide membranes | charged nanopore | nanofluidics | confinement effects

Pressure-driven membrane separation processes, such as reverse osmosis (RO) and nanofiltration (NF), have established themselves as the benchmark technologies for desalination. Significant improvements in membrane performance have been realized over the last 40 y as thin-film composite (TFC) polyamide membranes have emerged as the gold standard for NF and RO applications (1). Polyamide selective layers, formed through the interfacial polymerization of a diamine with a triacid chloride, offer tunable water–salt selectivity and high water permeability over a wide pH range, thus supplying excellent water quality at reduced energy costs (1, 2). NF, in particular, has emerged as a low-energy technology for separations of small molecules and divalent ions (3). However, inherent material limitations, such as susceptibility to scaling, fouling, and a permeability–selectivity trade-off, have constrained improvements in the performance of TFC polyamide membranes over the past decade (1, 2).

Polyamide networks contain carboxylic functional groups (R-COOH/R-COO[−]), formed from the hydrolysis of residual acid chlorides, and unreacted amines, following interfacial polymerization. These hydrophilic and ionizable moieties play an integral role in the performance of polymeric membranes. The extent to which a membrane is charged (i.e., its charge density) following the ionization of R-COOH and amine groups influences interactions between the membrane surface and charged constituents in the feed water, such as salts and natural organic matter (4). The importance of R-COO[−] in membrane performance typically

outweighs that of ionized amines due to the higher density of residual R-COOH in polyamide films (5, 6). Nevertheless, both can greatly influence the selectivity (7, 8), organic fouling (9), and scaling (10) of NF and RO membranes.

Despite the important role of charged groups in membrane performance, our understanding of the ionization of these functional groups within atomic-scale pores remains wanting. Charge density is a critical component in all models of nanofluidic transport across NF and RO membranes (7, 8, 11, 12). Essentially all models assume constant functional group ionization across the film (7, 11, 12), but this assumption is questionable as recent evidence suggests that R-COOH does not ionize uniformly in polyamide films (4, 5, 13–15). In particular, quantification of silver ions bound to R-COO[−] uncovered the existence of two separate acid dissociation constants, reported as pK_a values ($pK_{a,1} \sim 5.5$ and $pK_{a,2} \sim 9.5$), associated with R-COOH in nanoporous polyamide films. The pK_a shift has been proposed to be a result of different local environments experienced by R-COOH within the film, such as anomalously low dielectric constants or high proton concentrations of water confined by membrane pores (4, 13). We currently lack a clear consensus on the governing mechanism behind the ionization behavior of R-COOH in nanoporous films, making it unclear how R-COOH

Significance

Novel membrane processes and materials are needed to combat global water scarcity. The advancement of membrane materials for water purification processes such as desalination is hindered by our limited understanding of structure–property–performance relationships. We address this knowledge gap by elucidating the mechanisms which govern the ionization behavior of nanoporous polyamide films and their influence on membrane performance. Polyamide ionization is key to enhancing the separation efficiency of charged constituents in aqueous solutions. Our results illustrate that a large portion of the ionizable moieties in polyamide films remain uncharged during typical operation due to extreme confinement effects, thus going unutilized. Complete ionization of state-of-the-art polyamide membranes offers selectivity improvements that could markedly improve desalination process efficiency.

Author contributions: C.L.R., J.R.W., and M.E. designed experimental research; H.J.K. designed computational research; C.L.R. and Y.Z. performed experimental research; M.W., Z.Y., and H.J.K. carried out computational research; C.L.R., J.R.W., and M.E. analyzed data; C.L.R., M.W., and Z.Y. wrote the paper; and C.L.R., J.R.W., H.J.K., and M.E. edited the manuscript.

The authors declare no competing interest.

This article is a PNAS Direct Submission.

Published under the PNAS license.

¹To whom correspondence may be addressed. Email: menachem.elimelech@yale.edu.

This article contains supporting information online at <https://www.pnas.org/lookup/suppl/doi:10.1073/pnas.2008421117/-DCSupplemental>.

First published November 12, 2020.

will ionize during membrane operation. Given the paramount importance of charge density in membrane performance, gaining a fundamental understanding of R-COOH ionization could have vast implications on membrane operation, nanofluidic modeling, and novel membrane design.

In this work, we characterize the location-dependent charge density of nanoporous polyamide membranes and the impact of charge density on separation performance. Our analysis focuses on NF membranes, as Donnan exclusion generally plays a greater role in their performance than in RO membranes. To control film thickness, we extend the layered interfacial polymerization (LIP) technique to piperazine (PIP)-based polyamide TFC membranes, the state of the art for NF. Characterization of these films using the silver-binding method confirms the location-dependent behavior of R-COOH ionization in nanoporous polyamide films. We experimentally investigate the mechanisms governing R-COOH ionization behavior (i.e., local proton concentration or dielectric constant phenomena) and pair these insights with molecular dynamics (MD) simulations and density functional theory (DFT) to validate the mechanism behind the anomalous ionization behavior. We then evaluate the roles of fixed charged groups on the surface and within the film toward water-salt selectivity in NF. Finally, we assess the implications of our results for modeling nanofluidic transport through polyamide thin films, highlighting the intricate role of nanoconfinement effects and introducing opportunities for future membrane design.

Results and Discussion

LIP to Control Polyamide Film Thickness. We prepared several nanofilms of varying thickness (δ), with similar surface characteristics, to isolate changes in the interior R-COOH content, thus allowing direct comparison between the ionization behavior of R-COOH located on the surface and within the film. The validity of this technique holds only if physical—and chemical—similarity is preserved between the films, including the nanoporous structure. To accomplish this, we implemented an LIP technique to fabricate and compare PIP-based polyamide TFC membranes of varying thickness (Fig. 1A and *Materials and Methods*). Polyamide films fabricated by LIP are expected to maintain similar physicochemical characteristics, as the same reaction procedure was used sequentially (16).

Several techniques were used to characterize the polyamide films in an effort to validate the effectiveness of LIP. Depth profiles were measured via atomic force microscopy (AFM) of LIP-based polyamide films isolated on silicon wafers, with the selective layer of commercial NF270 membranes (DuPont Water) included for comparison (Fig. 1B and *SI Appendix, Fig. S1*). Selective layers for NF270 are formed by interfacial polymerization of PIP and trimesoyl chloride (TMC), suggesting similar chemistry as the LIP membranes. We found that the film thicknesses of the LIP membranes grew proportionally with the number of polyamide layers deposited. Specifically, the thickness of the LIP membranes increased from 25.5 ± 4.4 nm (1L PIP) to 111.5 ± 2.0 nm (5L PIP). The 1L PIP was approximately twice as thick as commercial NF270 ($\delta = 13.2 \pm 1.1$ nm).

We further imaged our LIP membranes by transmission electron microscopy (TEM) to corroborate the increase in membrane thickness with respect to the number of deposited polyamide layers (Fig. 1D–F). Our images highlight regions of isolated selective layers, where partial film detachment occurred during resin curing (17). The 1L PIP membrane displayed a thin, smooth structure (Fig. 1D) similar to previous observations of commercial NF270 (17). Increasing the number of layers during LIP consequently increased the membrane thickness from 25.3 nm (1L PIP) to 120.2 nm (5L PIP), as depicted in *SI Appendix, Fig. S2*, thus confirming observations from AFM. The 2L and 5L PIP membranes revealed some frayed sections of the

isolated polyamide films separated into distinct layers, which was likely an artifact of resin curing (17). The separation of the individual polyamide layers during resin curing suggests that the individual layers are connected via relatively weak physical interactions, similar to the connection between the base polyamide layer and the underlying polysulfone support (18).

Scanning electron microscopy (SEM) images of the LIP membranes illustrated small qualitative differences in the membrane surfaces (*SI Appendix, Fig. S3*). To quantify these morphological changes, we further analyzed the polyamide surface roughness via AFM. While there is an evident increase in the surface roughness with respect to film thickness (Fig. 1C), the surface roughness relative to the film thickness is quite low for all LIP membranes. More importantly, marginal differences in the relative surface areas of the films (1.05 to $1.19 \mu\text{m}^2/\mu\text{m}^2$ projected area; *SI Appendix, Table S1*) suggest that similar surface conditions are maintained.

To validate the LIP technique, we must also confirm that the LIP membranes possess analogous pore structures. Although microscopy allowed us to compare membrane surface morphologies and confirm our ability to scale film thickness with LIP, these techniques lack the resolution needed to resolve the nanoporous structure. With the use of the hindered transport model (HTM), we estimated the average pore size of the membranes from neutral organic solute rejection measurements (details in *SI Appendix, Fig. S4*). We found no statistically significant difference (z-test, $\alpha = 0.05$) in the average pore radii of the LIP membranes (0.570 to 0.585 nm), suggesting that the LIP technique does not alter the porous structure upon layer addition.

We further compared hydraulic water permeabilities (P_w^H) of our LIP membranes. In principle, P_w^H is a thickness-independent property that is governed by the physical confinement and chemical interactions experienced by water within the membrane pore (19). Therefore, it is reasonable to assert that similarities observed in the P_w^H of LIP membranes would be indicative of similar porous structures. To assess P_w^H , we measured the pure water permeability, or water permeance (A), of our LIP and NF270 membranes with a pressure-driven, cross-flow filtration system (Fig. 1G). We find A is inversely proportional to the selective layer thickness (i.e., $A \propto 1/\delta$), thus following (19)

$$J_w = A(\Delta p - \Delta \pi) = \frac{P_w^H}{\delta}(\Delta p - \Delta \pi), \quad [1]$$

where J_w is the water flux and Δp and $\Delta \pi$ are the hydraulic and osmotic pressure differences across the membrane, respectively. The P_w^H of the LIP membranes were obtained by normalizing permeance by their respective thicknesses (Fig. 1H). A P_w^H of $0.11 \pm 0.02 \text{ L } \mu\text{m} \cdot \text{m}^{-2} \cdot \text{h}^{-1} \cdot \text{bar}^{-1}$ was determined from fitting Eq. 1, which is roughly 10-fold greater than the permeability of *m*-phenylenediamine (MPD)-based polyamide nanofilms (16). MPD-based chemistry produces less permeable polyamide membranes than PIP-based films due to a tighter porous structure, which also yields substantially higher water-salt selectivity (20).

The constant water permeability, in conjunction with the precisely controlled film growth and similar pore size estimated by HTM, suggests that the deposited polyamide layers are similar from a chemical structure perspective. We note that this does not imply isotropic conditions throughout the films, as heterogeneities across each layer are still possible (6). Given our limited ability to characterize the porous structure beyond these techniques, similar porous structures of the LIP membranes, although likely, are not definite. NF270, on the other hand, displayed a significantly higher P_w^H ($0.27 \pm 0.02 \text{ L } \mu\text{m} \cdot \text{m}^{-2} \cdot \text{h}^{-1} \cdot \text{bar}^{-1}$). The difference in P_w^H between commercial NF270 and the hand-cast LIP membranes is likely the result of optimized manufacturing conditions of the active and support layers of NF270.

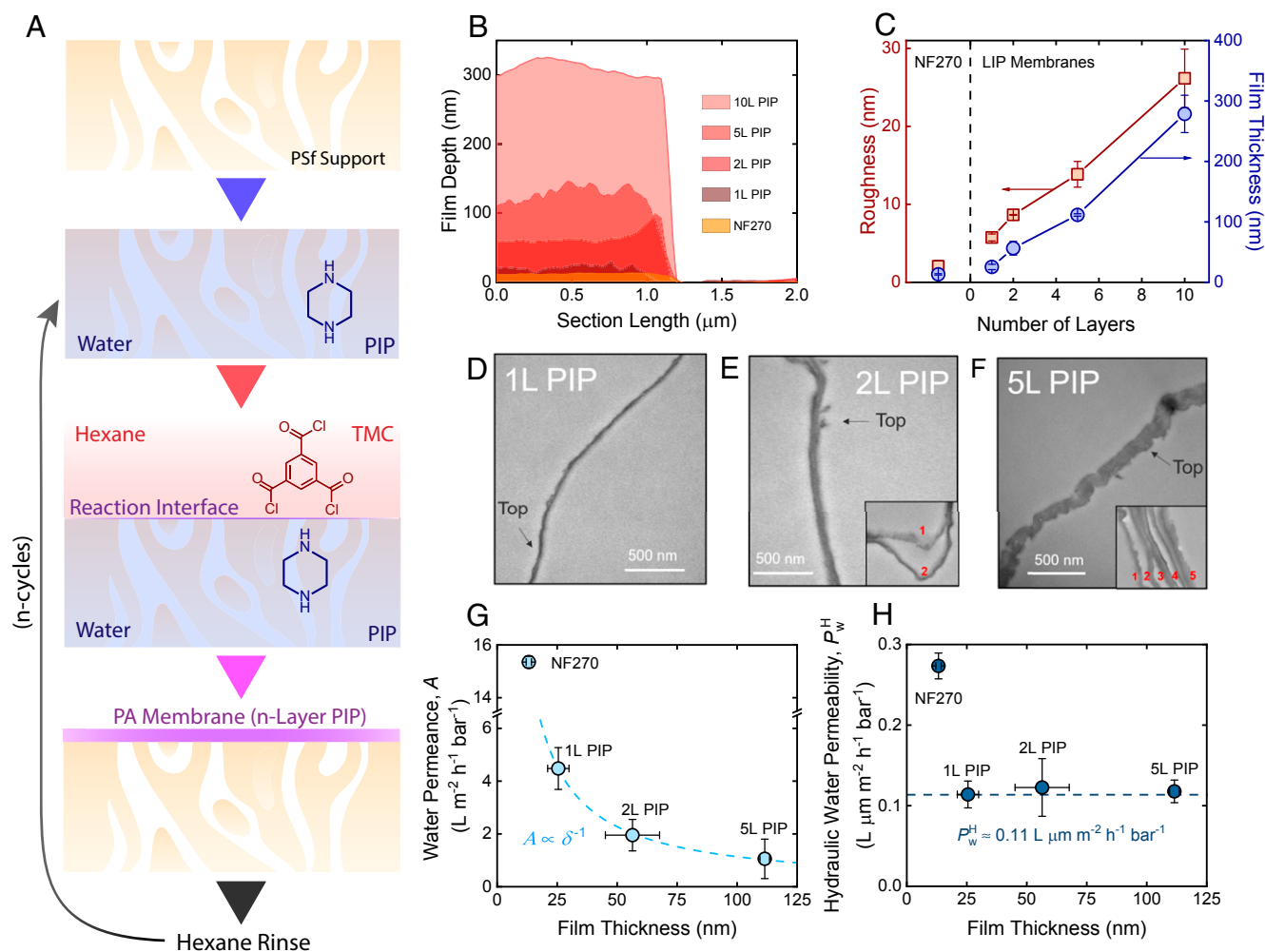


Fig. 1. LIP for NF membranes with controlled thickness. (A) Schematic of LIP process with PIP and TMC. (B) Average film depth profiles of LIP and NF270 membranes from AFM analysis over a $2\text{-}\mu\text{m} \times 1\text{-}\mu\text{m}$ segment. The segments used for AFM analysis can be found in *SI Appendix, Fig. S1*. (C) Analysis of thickness and roughness with respect to the number of PIP layers. NF270 was included for comparison. (D–F) TEM images of isolated (D) 1L, (E) 2L, and (F) 5L PIP selective layer cross-sections at 43,000 \times magnification. The top sides of the polyamide membranes, which are exposed directly to the feed solution, are indicated on the figures with arrows to provide clarity as to the orientation of the films. Insets in E and F depict the separation of individual polyamide layers in 2L and 5L PIP membranes. The frayed membrane selective layers illustrate the stacking of unique, similarly sized polyamide layers. (G) Water permeance, A , with respect to membrane thickness, δ . (H) Thickness-normalized hydraulic water permeability, P_w^H . All error bars represent one SD.

Differentiating Surface- and Interior-Based Carboxyl Groups.

Exploiting LIP to fabricate physically and chemically similar polyamide films of controlled thickness enables us to compare surface and interior R-COOH ionization. When comparing LIP membranes, surface R-COOH should remain roughly constant while interior R-COOH should scale linearly with film thickness (Fig. 24). If the proposed interpretation for R-COOH ionization is correct—where $pK_{a,1}$ represents R-COO $^-$ on the surface and $pK_{a,2}$ represents R-COO $^-$ throughout the entire film (i.e., surface and interior)—then only R-COO $^-$ associated with $pK_{a,2}$ should scale with thickness, while R-COO $^-$ associated with $pK_{a,1}$ would be independent of film thickness. Therefore, quantifying R-COO $^-$ with respect to solution pH for films of varied thickness will enable us to either validate or disprove this interpretation.

To quantify R-COO $^-$ throughout our LIP membranes, we bound and eluted silver ions, which were then quantified by inductively coupled plasma mass spectrometry (ICP-MS) (4). The R-COO $^-$ content of NF270 was also quantified for comparison. Areal R-COO $^-$ densities of the polyamide films (Fig. 2B), fitted by Eq. 2 found in *Materials and Methods*, illustrate two important findings for LIP membranes: 1) areal R-COO $^-$ densities associated

with $pK_{a,1}$ are low (0.3 to 0.9 sites per nm^2) and differences are statistically insignificant (one-way ANOVA, $\alpha = 0.05$) and 2) areal R-COO $^-$ density associated with $pK_{a,2}$ increases significantly for thicker polyamide films, increasing from 6.9 to 23.6 sites per nm^2 for 1L to 5L PIP membranes, respectively.

Complete R-COOH ionization is captured by a multi- pK_a model (Fig. 2D), which represents the superposition of the single- $pK_{a,1}$ and - $pK_{a,2}$ models. The single- $pK_{a,1}$ fits for areal R-COO $^-$ densities (dotted lines) overlap one another, indicating that R-COO $^-$ densities associated with $pK_{a,1}$ are independent of film thickness. Conversely, the single- $pK_{a,2}$ fits for R-COO $^-$ densities (dashed lines) illustrate a distinct thickness dependence. This is exemplified by directly comparing experimental R-COO $^-$ densities associated with $pK_{a,1}$ and $pK_{a,2}$ (Fig. 2E). R-COO $^-$ densities associated with $pK_{a,2}$ were isolated by subtracting out the contribution of R-COO $^-$ found at pH 7 (i.e., all R-COO $^-$ connected to $pK_{a,1}$) from the total R-COO $^-$ density at pH 10.5. In this case, areal R-COO $^-$ densities correlating with $pK_{a,2}$ scale proportionally to film thickness, while the R-COO $^-$ ionized at $pK_{a,1}$ remain relatively unchanged. Further normalizing pK_a -specific areal R-COO $^-$ densities by film thickness highlights that the LIP membranes have

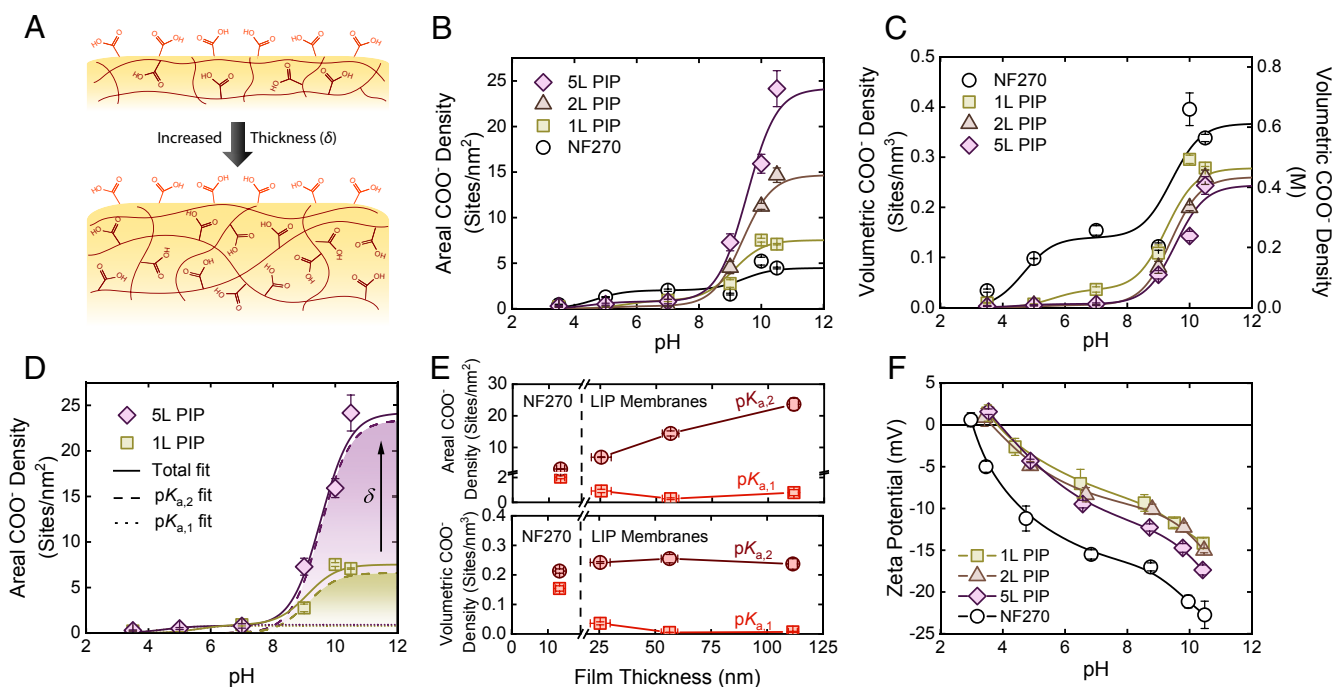


Fig. 2. Quantifying R-COO⁻ density in polyamide selective layers. (A) Illustration of hypothesized film growth during LIP, with areal R-COOH surface density and volumetric R-COOH interior density remaining constant. (B) Areal R-COO⁻ density as a function of pH for LIP membranes and NF270. (C) Volumetric R-COO⁻ density, representing the thickness-normalized active charge state of the membrane, as a function of pH for LIP membranes and NF270. (D) Impact of increased thickness on R-COO⁻ fitting. As illustrated for 1L and 5L PIP samples, increased thickness increases the pK_{a,2} intensity, while pK_{a,1} intensity remains constant. (E) Relative change in areal (Top) and volumetric (Bottom) R-COO⁻ densities with respect to membrane thickness for groups associated with the membrane surface (pK_{a,1}) and interior (pK_{a,2}). Interior R-COO⁻ density was determined by subtracting the surface R-COO⁻ density, measured at pH 7, from the total R-COO⁻ density, measured at pH 10.5. (F) Change in zeta potential with respect to pH for LIP membranes and NF270. All error bars represent one SD.

similar volumetric densities (0.24 to 0.25 sites per nm³ or 0.4 to 0.41 M) of R-COOH associated with pK_{a,2} (Fig. 2E). These densities are similar to those of commercial fully aromatic polyamide membranes, which exhibited R-COO⁻ densities of 0.2 to 0.6 M (4, 15).

Membrane zeta potential was evaluated by streaming potential measurements (*Materials and Methods*) as another indicator of surface charge. Although this method does not provide a quantitative charge density, it captures the relative ionization state at the membrane surface (21). Thus, zeta potential is useful for comparing the surface charge of different membranes. At pK_{a,1} (i.e., pH 5), the zeta potentials of the LIP membranes closely overlap, while NF270 exhibits a much greater negative charge (Fig. 2F). This behavior mirrors trends for pK_{a,1} in Fig. 2B and corroborates our previous finding: pK_{a,1} is independent of film thickness. We also note the appearance of a second pK_a located around pH 9, which indicates that a small amount of interior R-COO⁻ contributes to the streaming potential measured at high pH (detailed analysis is provided in *SI Appendix*, Fig. S5).

Our analysis of LIP membranes, which exemplifies the unique ionization behavior of nanoporous polyamide films, verifies that the separate pK_a values distinguish surface and interior R-COO⁻. In other words, the thickness dependence of R-COOH ionization at pK_{a,2}, paired with the unchanging ionization behavior at pK_{a,1}, strongly supports the location-dependent interpretation behind R-COOH ionization—pK_{a,1} represents only surface R-COO⁻, whereas pK_{a,2} represents all R-COO⁻ throughout the film. Following this framework, comparison of the two pK_a populations for NF270 with LIP membranes shows comparable volumetric densities of interior R-COO⁻ (Fig. 2E). In contrast, the surface of NF270 is far more carboxyl-rich than the LIP membranes (Fig. 2E). Disparity between surface R-COOH densities may be the result of

additional posttreatment techniques during NF270 fabrication to enhance surface charge (22).

Shift in pK_a is Mainly due to Lower Dielectric Constant within Polyamide Pores. Ionization of the functional groups present in polyamide networks formed from PIP-based chemistry depend on local conditions of the pores. In particular, the local proton concentration and dielectric constant of a hydrated polymer matrix play critical roles in the ionization of weak-acid functional groups such as R-COOH (23, 24). Disparity between local conditions (i.e., proton concentration or dielectric constant) within a pore and the bulk solution can shift the observed pK_a of functional groups positioned in the pores. The local proton concentration phenomenon is classically observed for ion exchange (IEX) resins at low ionic strength, where the proton concentration within the pores is higher than the bulk solution as protons act as counterions to satisfy electroneutrality (23). The increase in local proton concentration within a negatively charged pore can be further exacerbated by confinement effects (25). Extreme confinement may also influence dielectric interactions. Theoretical analyses of dielectric phenomena influencing ion transport indicate that confined charged groups fixed to dielectric walls have stronger electrostatic interactions with available counterions than in the bulk (26). Thus, a substantial decrease in local permittivity makes it less favorable for ionogenic groups to dissociate as their electrostatic charge is less readily stabilized by their surroundings (26, 27).

The presence of local proton concentration effects can be assessed by modulating the ionic strength of the solution (23). The addition of a salt which can penetrate the pore results in the

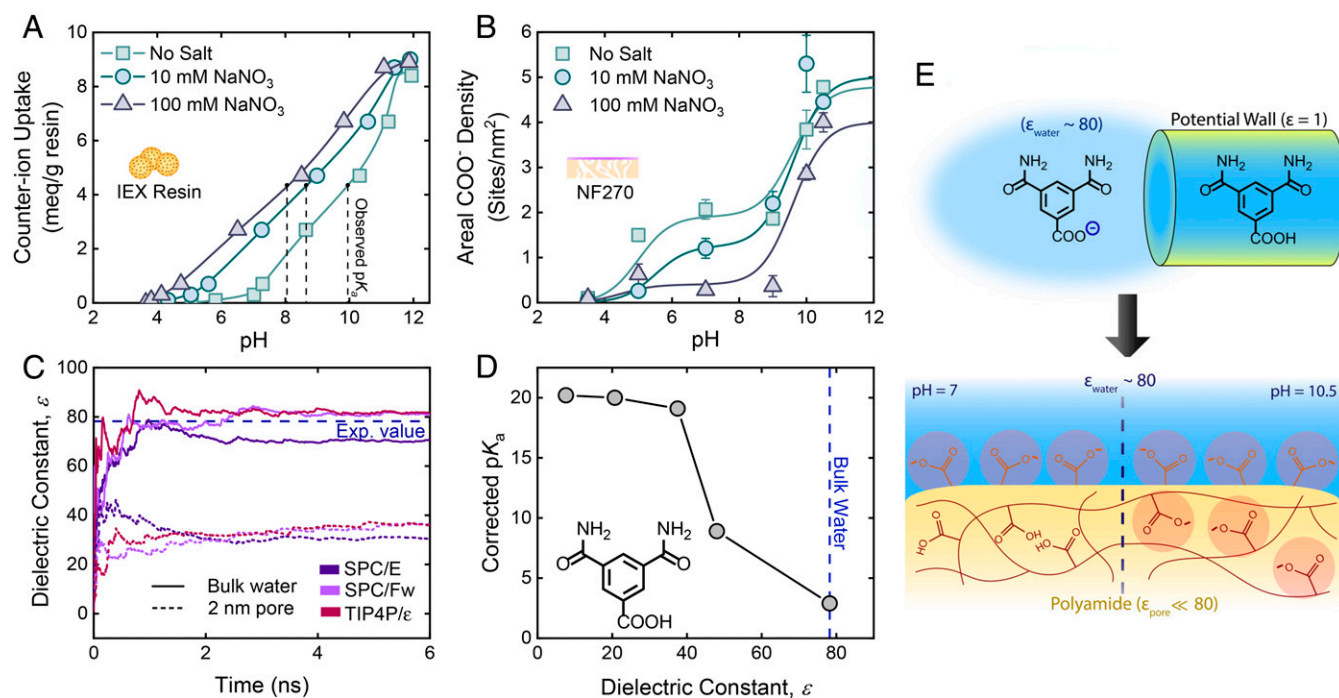


Fig. 3. Elucidating the mechanisms behind R-COOH ionization. (A) Shift in observed pK_a of a carboxylate-based IEX resin due to ionic strength. (B) Effect of ionic strength on the charge state of R-COOH in NF270. Leftward shifts in the observed pK_a with respect to ionic strength were not seen. (C) MD simulations of the dielectric constant of bulk and nanoconfined water by the rigid three-site SPC/E, flexible three-site SPC/Fw, and rigid four-site TIP4P/ ϵ water models. (D) Relation between the pK_a of a polyamide-based R-COOH analog (3,5-dicarbamoylbenzoic acid) and the dielectric constant of the surrounding media determined by DFT. (E) Relating theoretical insight on dielectric-driven ionization to practical implications. Nanoconfinement of water by a low-permittivity media changes the ionization behavior of R-COOH due to reduced charge stability, measured by enhancements in its pK_a (Top). The lower local dielectric constant of confined water found in low-permittivity polyamide pores prevents R-COOH ionization at neutral pH (Bottom Left), whereas at high pH (Bottom Right) the local proton concentration decreases enough to stabilize the excess charge needed for R-COOH ionization. Although depicting a molecularly thin surface, the surface layer likely has some meaningful thickness. All error bars represent one SD.

displacement of protons associated with the functional groups by the newly introduced cations, which thereby shifts the observed pK_a closer to the apparent pK_a of the functional groups (23). We have demonstrated this by titrating a carboxylate-based IEX resin with varying ionic strength solutions (Fig. 3A). In deionized water, the observed pK_a of the IEX resin (~ 10) was similar to $pK_{a,2}$ of our polyamide films (~ 9.5). The observed resin pK_a shifted toward the apparent pK_a of R-COOH (~ 5) upon the introduction of salt in solution.

Using a similar approach, we examined the effect of various ionic strengths on the areal R-COO⁻ density of NF270 measured by the silver binding method. Our results show that changing the ionic strength had little to no effect on the observed $pK_{a,2}$ of NF270 (Fig. 3B). The only differences were decreased NF270 R-COO⁻ densities associated solely with $pK_{a,1}$ at higher ionic strengths. The decrease in the R-COO⁻ density is attributable to overscreening by Na⁺, preventing silver ions from accessing R-COO⁻ sites. Poor NaNO₃ rejection by the NF270 membrane ($< 43\%$) across all pH values suggests that sodium was able to access interior R-COO⁻ due to adequate film penetration (SI Appendix, Fig. S6). Although our results do not conclude an absence of higher local proton concentrations in polyamide films, they do confirm that the pK_a shift found in polyamide films is driven by a different phenomenon. Additionally, our results illustrate that the silver-binding method appears to describe the actual ionization of R-COOH during real operation, including at higher ionic strengths more typical of desalination feed streams. In other words, at neutral pH surface R-COOH groups are ionized, while the interior R-COOH are not.

The lack of a local proton concentration effect suggests that a lower local dielectric phenomenon is the most plausible cause for

the appearance of two pK_a values in TFC polyamide membranes. We investigated the possibility of confinement-induced dielectric effects on the ionization of R-COOH by MD simulations and DFT as described in *Materials and Methods*. In particular, we applied MD simulations to assess the effect of nanoconfinement by a low-permittivity medium on the local dielectric constant of water. Several water models (e.g., SPC/E, SPC/Fw, and TIP4P/ ϵ) were used to simulate water clusters and interactions, calculating the dielectric constant from the fluctuation in the water dipole moment along the MD trajectory (Eq. 4). Using this method, we calculated dielectric constants for bulk water that ranged from roughly 71 to 82, which is in good agreement with its measured value ($\epsilon_{\text{water}} = 78.2$) and validates our protocol for computing dielectric constants (Fig. 3C).

To induce confinement effects representative of the membrane pore, we constrained the water molecules by cylindrically shaped potential walls with a diameter of 2 nm (SI Appendix, Figs. S7 and S8). Constraining water by harmonic potential boundaries represented the simplest route to achieve the purpose of this simulation, namely, to demonstrate the intrinsic influence of confinement on the local dielectric constant of water (details in SI Appendix). The simulation was allowed to reach steady-state conditions (6 ns). An evident decrease in the dielectric constant of water from its bulk value was observed (Fig. 3C), as the confined water molecules displayed a dielectric constant approximately twofold less than bulk water ($\epsilon \approx 30$ to 37). These simulations support the ability of a low-permittivity medium, such as polyamide ($\epsilon \approx 3$) (7), to reduce the local dielectric constant of water upon extreme confinement. For comparison, previous experimental characterization and transport modeling of polyamide NF

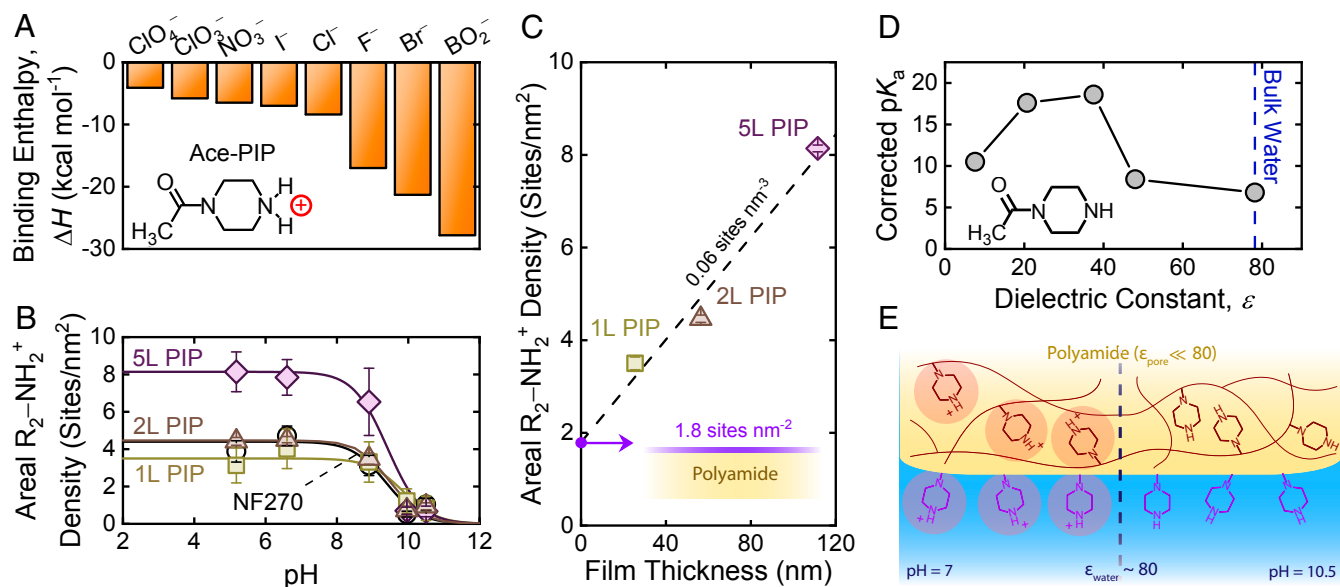


Fig. 4. Quantifying $R_2-NH_2^+$ in semiaromatic polyamide membranes. (A) Binding enthalpies between a polyamide-based piperazine analog, Ace-PIP, and probe anions gathered from DFT calculations. (B) Areal $R_2-NH_2^+$ density, representing the active positive-charge state of the membrane, as a function of pH for the LIP and NF270 membranes. PIP ionization behavior follows a single- pK_a fit, exhibiting a pK_a of ~ 9 , and was measured through binding Br^- counterions. (C) Areal $R_2-NH_2^+$ density with respect to LIP film thickness, where the intercept and slope correspond to the $R_2-NH_2^+$ density of the surface and the interior, respectively. The total areal $R_2-NH_2^+$ densities used to fit the single- pK_a models in B were used for this analysis. (D) Role of media dielectric constant, determined by DFT, on the pK_a of Ace-PIP. (E) Illustration of operationally dependent PIP ionization in semiaromatic polyamide films. PIP groups within the film possess the same ionization state as those on the surface due to negligible differences between their pK_a values. Although depicting a molecularly thin surface, the surface layer likely has some meaningful thickness. All error bars represent one SD.

membranes found dielectric constants within the membrane pores to be 20 to 50, loosely matching our simulation results (7, 28)

DFT was then applied to evaluate the role of the intermediate dielectric constant in the ionization of semiaromatic polyamide-based $R-COOH$. To reduce the complexity of modeling a highly cross-linked polymer network, we selected 3,5-dicarbamoylbenzoic acid as a truncated molecular model of polyamide to study $R-COOH$ ionization. We modeled the ionization of our $R-COOH$ analog via DFT in solvents of varying dielectric constant and then corrected the calculated pK_a values based on experimental values of benzoic acid (Fig. 3D and Materials and Methods). We observed a notable increase in the corrected pK_a values of 3,5-dicarbamoylbenzoic acid experiencing lower dielectric constant, corroborating the viability of a dielectric-driven mechanism behind the upward shift in $R-COOH$ pK_a .

Our theoretical simulations of a polyamide-based $R-COOH$ analog suggest a possible mechanistic framework behind the ionization behavior of nanoporous polyamide films (Fig. 3E). Bulk water presents a favorable medium for $R-COOH$ ionization, where highly polarizable water molecules can readily stabilize the electrostatic charge of $R-COO^-$ at neutral pH. However, extreme confinement induces ordering of water molecules that reduces their ability to polarize and thus decreases their dielectric constant (29). This confinement-based phenomenon has been observed in other areas of study, including polyelectrolyte interactions (30), protein electrostatics (31), and solid-state nanofluidics (29). The added difficulty for confined water—exhibiting a low local dielectric constant—to stabilize excess electrostatic charge is of particular importance in these subject areas as it can influence the structural and thermodynamic properties of the system as well as ion interactions. Relevant to our study, the lower local dielectric constant consequently increases the pK_a of $R-COOH$ within single-digit nanopores. For nanoporous polyamide membranes, only $R-COOH$ groups experiencing bulk water conditions are expected to ionize at neutral pH. $R-COOH$ located in large pores $\gg 2$ nm or on the surface of the membrane would satisfy these conditions. However,

considering that polyamide NF membranes comprise pores almost solely below 2 nm (32), the latter case is more tenable.

Ionization of Piperazine-Based Amine Groups. Similar to $R-COO^-$, positively charged amine groups can impart hydrophilicity and influence electrostatic interactions between the membrane and charged constituents in the aqueous solution. Therefore, it is important to understand amine ionization when considering water and ion transport across nanoporous polyamide films. To our knowledge, the amine content and ionization of polyamide films has been quantitatively addressed in just one study (13). In this study, tungstate (WO_4^{2-}) was used as a probe to quantify ionized amine groups in fully aromatic polyamide NF and RO membranes (13), revealing a pK_a of ~ 4.1 (characteristic of aniline) and a low density relative to carboxylic groups.

WO_4^{2-} is not an ideal probe for polyamide films, including PIP-based NF membranes, as it is a large ion that may not be able to access many $R_2-NH_2^+$ sites within the membrane. Furthermore, the stoichiometric binding ratio between an ionized amine and the divalent WO_4^{2-} is unclear, making it difficult to interpret data. Therefore, to quantify $R_2-NH_2^+$ in our membranes, we employed DFT calculations to predict which monovalent anions would express the most favorable binding (Fig. 4A). Binding favorability was quantified by the binding enthalpy (ΔH) between the anion and acetylated piperazine (Ace-PIP), which we selected as the molecular analog for $R_2-NH_2^+$ in polyamide films. DFT revealed metaborate (BO_2^-) binds the most favorably with Ace-PIP; however, due to the tendency of metaborate's conjugate acid to form metaboric acid, BO_2^- was considered unsuitable for quantifying $R_2-NH_2^+$ over a wide pH range. As such, bromide (Br^-) was selected as the most suitable counterion for probing R_2-NH ionization. The same bind-and-elute technique used for determining $R-COO^-$ content was adopted here but with slight modifications (Materials and Methods).

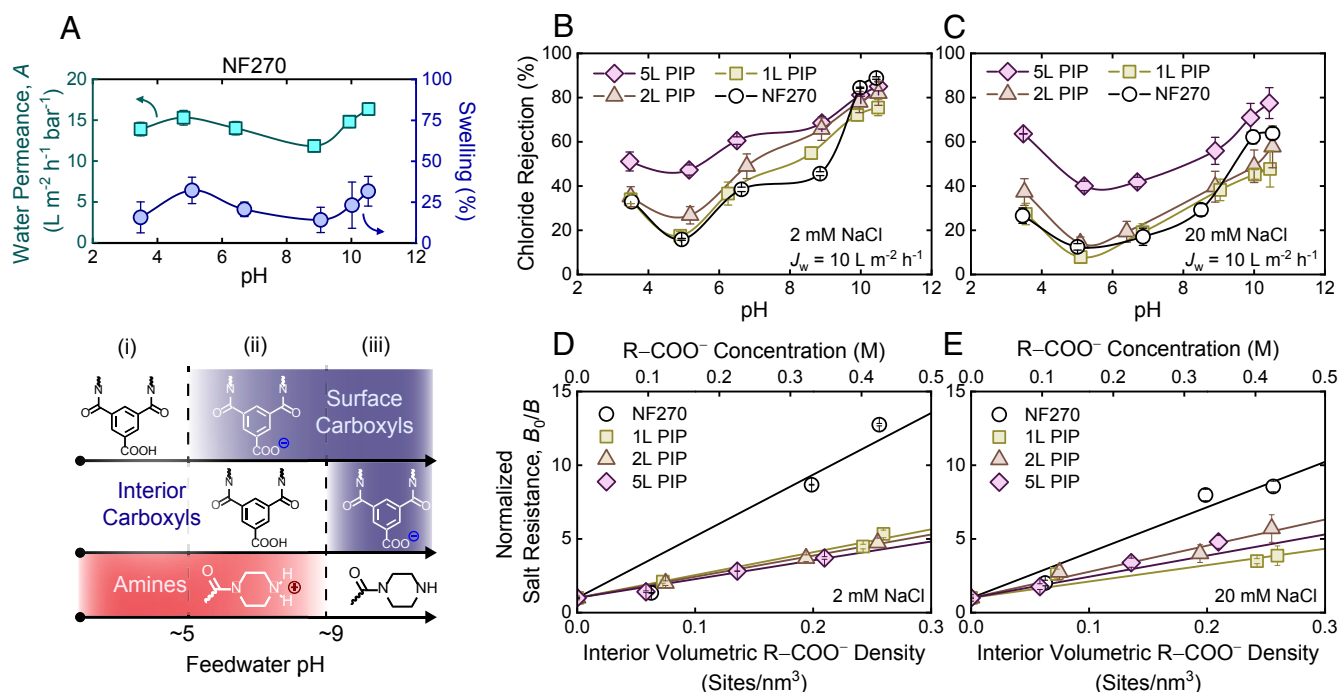


Fig. 5. Influence of R-COOH and R₂-NH ionization on membrane swelling and performance. (A) Change in the pure water permeability coefficient and swelling of NF270 with respect to solution pH (Top). Starting from pH 7, the solution pH was decreased to pH 3.5 by HCl addition before being incrementally increased to pH 10.5 by NaOH. Swelling of the polyamide layer, which was quantified by the relative change in wet film thickness compared to the dry film, can be ascribed to the (de)ionization of R-COOH and R₂-NH throughout the membrane (Bottom). (B and C) Dependence of solute rejection on the number of sequential PIP layers and pH for (B) 2 mM and (C) 20 mM NaCl feed solutions. Measurements for all feed solutions were collected under a constant water flux ($J_w = 10 \text{ L m}^{-2} \text{ h}^{-1}$) to mitigate differences in concentration polarization between membranes of varying permeability. (D and E) Increase in salt resistance, taken as the inverse salt permeance (i.e., B^{-1}), related to ionization of interior R-COOH groups at (D) 2 mM and (E) 20 mM NaCl. Results are based on measurements found in B and C. The interior volumetric R-COO⁻ density was determined by subtracting the surface R-COO⁻ density, measured at pH 7, from the ionized R-COO⁻ densities measured above pH 7. Salt resistances were normalized to the salt resistance at pH 7 (B_0^{-1}) to assess the sole influence of interior R-COO⁻ on salt transport. All error bars represent one SD.

Areal R₂-NH₂⁺ densities of the LIP and NF270 membranes illustrate single- pK_a ($pK_a \sim 9.5$) ionization of R₂-NH (Fig. 4B), similar to that of the simple analog piperidine (pK_a of ~ 11). The lack of multiple pK_a values suggests that the difference observed between the ionization of surface and interior R-COOH does not hold for R₂-NH. In this case, R₂-NH₂⁺ densities would be representative of the total R₂-NH content (i.e., surface and interior). The roughly constant value for Br⁻ uptake below pH 7 also suggests that the counterion probe is associating with ionized amine groups rather than being cosorbed alongside protons, as has been recently proposed for fully aromatic polyamides (33–35). If proton uptake was the predominant means by which Br⁻ was associated into the membrane, one would instead expect an exponential increase in Br⁻ uptake as pH decreases.

We find consistently less total R₂-NH than R-COOH in LIP membranes, which is expected for polyamide films (20, 36). The disproportionate scaling between total R₂-NH content and film thickness in our LIP membranes likely stems from the grouped contributions of surface and interior R₂-NH₂⁺. By plotting total R₂-NH content against film thickness (Fig. 3C), we can extract the surface R₂-NH density from the y-intercept (1.8 sites per nm²). We note that most of the surface R₂-NH are likely present on the bottom surface of the membrane, based on the orientation of the interfacial polymerization reaction (20, 36). The slope of the line suggests an interior amine density of 0.06 ± 0.01 sites per nm³ (or $0.10 \pm 0.02 \text{ M}$). R₂-NH and R-COOH contents were similar in NF270, and we are unable to distinguish surface and interior R₂-NH in this case.

Results from Fig. 4B imply that decrements to the local dielectric constant within the polyamide pore have negligible effect

on the charge stability of R₂-NH₂⁺. DFT calculations on the ionization of Ace-PIP in solvents of varying dielectric constant support this notion (Fig. 4D). Specifically, the projected increase (rather than a decrease) in the pK_a of Ace-PIP at lower dielectric constants indicates that lower-permittivity media do not inhibit R₂-NH ionization. In other words, Ace-PIP can remain ionized over a wide pH range—regardless of its dielectric environment. This theoretical insight reinforces the notion that R₂-NH ionization behavior for varying pH is similar across the film thickness (Fig. 4E).

Influence of Ionization on Membrane Performance. The added hydrophilicity and exclusion of coions that coincide with R-COOH and R₂-NH ionization are inextricably linked with membrane performance. The enhanced hydrophilicity of ionized groups typically increases water uptake by the polymer matrix, leading to swelling and increased water permeability (19). In general, polymers that absorb more water also absorb more salt, leading to a permeability-selectivity trade-off where higher water permeability comes at the cost of reduced water-salt selectivity (37). The swelling behavior of polyamide thin films was previously reported to be pH-dependent (38), but this was largely based on the comparison of just two data points. The bulk of membrane research still lacks a thorough investigation into the pH-dependent swelling behavior of polyamide thin films and its subsequent influence on membrane performance.

Feed solution pH should only influence the ionization of fixed functional groups throughout the film. Therefore, interpreting the effect of pH from an ionization perspective is reasonable. We assessed the effect of pH—and consequently membrane charge—on the swelling and water permeability of NF270 (Fig. 5A). We find the observed trends in water permeability coincide remarkably well with

the swelling of the NF270 selective layer, measured by comparing nanofilm thickness in liquid water with thickness in air (Fig. 5A). Our data suggest that polyamide swelling can be interpreted by breaking R-COOH and R₂-NH ionization into three stages: 1) pH < 5, 2) pH 5 to 9, and 3) pH > 9. In the first stage (pH < 5) there is no change in R₂-NH ionization (i.e., all are R₂-NH₂⁺), which accounts for most of the swelling. As the solution pH approaches 5, the gradual ionization of surface R-COOH causes electrostatic repulsion between R-COO⁻ near each other, thus increasing the swelling from 15.7 to 32.2%. Entering the second stage (pH 5 to 9), surface COOH are fully ionized. During this stage, the hydrophilicity of the membrane decreases as R₂-NH₂⁺ gradually deprotonate, thus reducing the swelling to 14.2%. For the final stage (pH > 9), R₂-NH₂⁺ have completely deprotonated (i.e., all are R₂-NH), while interior R-COOH are subsequently ionized. Despite the neutralization of the amines, the introduction of a high density of hydrophilic R-COO⁻ increases film swelling sharply to 31.7%. The pH-dependent swelling measurements reported here are qualitatively similar to vapor swelling of semiaromatic polyamide selective layers (20 to 45% at 95% relative humidity), measured using X-ray reflectivity (39). While the observed trends in water permeability and swelling appear to mirror each other, the change in swelling does not produce a 1:1 change in water permeability. For instance, the roughly twofold increase in swelling (15.7–32.2%) from pH 3.5 to pH 5 results in a 10% increase in the water permeability, which runs counter to typically large increases in permeability with increased water sorption (19). The limited effect on permeability may be due to heterogeneous swelling behavior, such as localized swelling near the top surface with minimal change in the dense center of the nanofilm, owing to the nonuniform ionization behavior.

The salt separation efficacy of the LIP and NF270 membranes was assessed in a cross-flow filtration system (Fig. 5B and C). All membranes were tested under a constant water flux ($J_w = 10 \text{ L}\cdot\text{m}^{-2}\cdot\text{h}^{-1}$) in an effort to maintain similar solute boundary layers at the membrane–solution interface for membranes of varying water permeability. Chloride (Cl⁻) rejection of 2 mM NaCl feed solution from pH 3.5 to pH 9 (Fig. 5B) mirrored trends observed in previously published works on NF separation (40, 41). Below pH 5, Cl⁻ rejection is governed via Na⁺ exclusion by R₂-NH₂⁺ to maintain solution electroneutrality. As the pH increases to 5, NaCl rejection approaches a minimum with the ionization of surface R-COOH. Diminished Cl⁻ rejection at this point likely stems from increased salt sorption into the membrane due to the high degree of swelling at pH 5 (19). Cl⁻ rejection did not increase substantially until pH > 9, where the deprotonation of R₂-NH₂⁺ and interior R-COOH greatly enhanced Cl⁻ exclusion. To our knowledge, this behavior has not been observed until now, likely due to the lack of published rejection data beyond pH 9 (21, 41, 42). Trends in Cl⁻ rejection generally mirror the opposite behavior of membrane swelling and appear to be explained well by R₂-NH and R-COOH ionization.

From the solution–diffusion model, the salt flux, J_s , can be represented as $J_s = B\Delta c$, where B is the salt permeance and Δc is the salt concentration difference across the active layer. The salt permeance can be considered as the reciprocal of salt resistance, R_s , across the membrane (i.e., $R_s = B^{-1}$) (43). Based on the rejection data presented in Fig. 5B, we determined salt permeance (SI Appendix, Fig. S9) and the corresponding salt resistance (SI Appendix, Fig. S10). The overall resistance increased 4- to 13-fold from pH 7 to pH 10.5, suggesting that interior R-COO⁻ groups play a prominent role in salt separation at high pH. We further compared the normalized salt resistance of our LIP and NF270 membranes against interior volumetric R-COO⁻ densities (Fig. 5D and E). Resistances (i.e., B^{-1}) were normalized to the salt resistance at pH 7 (i.e., B_0^{-1}), where interior R-COOH groups remain neutrally charged. Our data suggest that salt resistance increases linearly with R-COO⁻ density. This behavior matches relevant models that

describe ion transport in NF and RO membranes (e.g., steric–dielectric–Donnan and ion association models) (44, 45). While these models are principally different, in the limiting forms for high coion exclusion, both relate salt permeance to the volumetric charge density of the film, X , by $B \propto X^{-n}$. The value of n depends only on the symmetry of the electrolyte (i.e., n describes the ratio of counterions to coions in the salt). For the monovalent, symmetric electrolytes studied here, our data suggest that $n \approx 1$ under the given experimental conditions, which agrees with the physical interpretation of n . More work is needed to elucidate which model is most appropriate to explain the transport mechanisms across nanoporous polyamide. Experimental insight from this study may provide further clarity.

Implications for the Design of Desalination Membranes. Our work demonstrates the intricate relationship between polyamide ionization, film morphology, and membrane performance. While understanding the unique ionization of nanoporous polyamide films was the primary goal of our study, it is increasingly apparent that an improved understanding of polyamide ionization can help develop fundamental structure–property–performance relationships. Such frameworks could lead to improved nanofluidic transport modeling and novel membrane design.

Insufficient understanding of R₂-NH and—more importantly—R-COOH ionization in nanoporous polyamide films is evident in nearly all ion transport models for NF and RO. The effective charge density is a critical component in these models; however, most models assume homogeneous functional group ionization across the entire film, regardless of pH (7, 11, 12). Our work highlights the critical flaws in current models, which do not account for the separate ionization of the polyamide surface and pore, while also introducing the techniques and experimental benchmarks necessary to improve them. Quantifying R-COO⁻ densities on the membrane surface and interior will establish more realistic frameworks for transport modeling, thus improving our comprehensive understanding of nanofluidic transport across polyamide NF and RO membranes.

Charge-based exclusion is broadly recognized as a primary rejection mechanism for NF membranes and has commonly been exploited to improve NF performance (21, 40, 42). While the influence of charge-based exclusion on membrane performance has primarily been conceptualized as a surface-based phenomenon (7, 21, 41), our findings suggest that interior R-COOH could play a significant role if ionized. Notably, we find the complete ionization of interior R-COOH results in a greater than fourfold increase in the water–salt permselectivity of NF270 (SI Appendix, Table S2 and Fig. S11). This fundamental insight has important implications for future membrane design. Furthermore, similarities observed in the R-COOH ionization behavior of fully aromatic polyamide RO membranes indicate that comparable performance enhancements could be exploited in brackish water RO (4).

Although these proposed benefits are intriguing, desalination typically occurs far below pH 10.5 (usually around pH 8) (3), where interior R-COOH would not ionize. Therefore, the advantage of interior R-COO⁻ cannot be captured under typical operating conditions given current membrane materials. Several methods may be available to increase the effective charge density within TFC membranes at operationally relevant pH. Increasing the membrane pore size could increase the local dielectric constant, allowing R-COOH to ionize more readily. However, this would come at a significant cost to steric hindrance of solutes. Likely more feasible is the tailoring of membrane pores with highly acidic functional groups (e.g., sulfonate) that will readily deprotonate in most environments (generally $pK_a < 1$) (46). Incorporating sulfonate groups into polymers has been a popular route for introducing additional charge and hydrophilicity (19). While the added charge in the membranes studied here resulted in increased water permeability and water–salt selectivity, sulfonation of polymers has produced

mixed results (19). The addition of excessive charge can lead to significant swelling and, consequently, reduced salt exclusion. This trade-off necessitates a balance, where enough fixed charges must exist to exert sufficient resistance to ion mobility and maintain adequate salt exclusion without overswelling the polymer matrix.

Materials and Methods

LIP. Layered TFC NF membranes were fabricated by forming several sequential polyamide selective layers atop prewetted PS20 (Sepro) support membranes via LIP (*SI Appendix*), a method previously used for polyethyleneimine- and MPD-based TFC membranes (16, 47). The aqueous amine solution used for forming the polyamide layer consisted of 1.0 wt % PIP, 0.5 wt % triethylamine, and 0.15 wt % NaOH in deionized water. We denote our layered membranes as “nL PIP,” where n represents the number of PIP-based polyamide layers deposited on the membrane.

Material Characterization of Polyamide Films. SEM (10 kV SU8230; Hitachi) was used for qualitatively analyzing the surface morphology and roughness of the film. Membrane samples were sputter coated with 2 nm of iridium (208HR Sputter Coater; Cressington) to prevent charging. Images were captured at 10,000× magnification. TEM was performed with an FEI Tecnai G2 Spirit BioTWIN to analyze cross-sectional features of the polyamide film. An 80-kV electron source was applied with a LaB6 filament. Samples were microtomed prior to TEM imaging (*SI Appendix*).

The film thickness and roughness of isolated polyamide films were quantified via AFM (*SI Appendix*) based on previously published methods (38, 48). A 10L PIP membrane was fabricated only for AFM analysis to substantiate the relationship between the number of deposited layers and the membrane thickness. Image analysis was performed with Nanoscope Analysis v1.9 (Bruker) software. The same method used to quantify film thickness in AFM was extended to determine swelling in the polyamide film (details in *SI Appendix*). After measuring the dry film thickness (δ_d), we pipetted water of controlled pH (ranging from pH 3.5 to 10.5) onto the film. We allowed the film to equilibrate at each pH (~5 min) before measuring the thickness of the swollen film. Swelling was calculated as the relative change in thickness of the wet film (δ_w) compared to the dry film, $(\delta_w - \delta_d)/\delta_d$.

Quantification of Ionized Carboxyl and Amine Functionalities. The silver-binding/ICP-MS method (details in *SI Appendix*) was employed to determine R-COO[−] throughout the polyamide film (4). We did not remove the fabric backing of the LIP membranes in an effort to avoid altering their R-COOH density. Instead, we calibrated our measured values by subtracting the average silver quantity found in our control support membranes (*SI Appendix*, Fig. S12). The same procedure was repeated when assessing amine ionization, but with slight modifications (*SI Appendix*).

ICP-MS (ELAN DRC-e; PerkinElmer) was utilized to quantify eluted silver, using a calibration curve ranging from 0 to 200 $\mu\text{g}\cdot\text{L}^{-1}$. Indium nitrate (40 $\mu\text{g}\cdot\text{L}^{-1}$) was used as the internal standard. Ion chromatography (930 Compact IC Flex with Metrosep A Supp 5-150/4.0 column and conductivity detector; Metrohm) was used to analyze eluted bromide, using a calibration curve ranging from 0 to 100 $\mu\text{g}\cdot\text{L}^{-1}$. Counterion concentrations were converted to areal R-COO[−] and R₂-NH₂⁺ densities (*SI Appendix*). Carboxyl and amine ionization were fitted using multi-pK_a and single-pK_a functions, respectively (4, 5):

$$[\text{R} - \text{COO}^-] = C_{\text{T,R-COOH}} \sum_{i=1}^n w_i \frac{K_{a,i}}{[\text{H}^+] + K_{a,i}} \quad [2]$$

$$[\text{R}_2 - \text{NH}_2^+] = C_{\text{T,R}_2-\text{NH}} \frac{[\text{H}^+]}{[\text{H}^+] + K_a} \quad [3]$$

where $C_{\text{T,R-COOH}}$ and $C_{\text{T,R}_2-\text{NH}}$ are the total densities of residual carboxyl and amine groups throughout the film, $[\text{H}^+]$ is the molar proton concentration,

K_a is the acid–base equilibrium constant, and w is the fraction of groups with different K_a . Two K_a values (i.e., $n = 2$) were used to fit carboxyl ionization for the polyamide membranes.

The zeta potential of the membrane surface was evaluated by a streaming potential analyzer utilizing an asymmetric clamping cell (EKA; Brookhaven Instruments) as reported previously (49). Measurements were performed with a solution containing 1 mM potassium chloride (KCl) and 0.1 mM potassium bicarbonate (KHCO₃). The streaming potential induced by flowing the electrolyte solution over the membrane surface at pressures ranging from 0 to 300 mbar was measured using Ag/AgCl electrodes mounted at each end of the clamping cell.

A carboxylate-based weak acid IEX resin (Dowex MAC-3; DuPont) was used to demonstrate the effect of ionic strength on carboxylate pK_a (*SI Appendix*), as shown previously (23).

First-Principles Simulations of Dielectric Phenomenon. Classical MD simulations were performed to determine the dielectric constant of bulk and confined water using the LAMMPS (50) (7 Aug 2019) package (details in *SI Appendix*, Table S3 and Fig. S13). The dielectric constants of bulk and confined water models were computed using the PyLAT (51) package from the fluctuations of water dipole moments along the trajectories from the 6 ns of production dynamics according to

$$\epsilon = 1 + \frac{\langle M^2 \rangle - \langle M \rangle^2}{3\epsilon_0 V k_B T}, \quad [4]$$

where T is the absolute temperature, k_B is the Boltzmann constant, V is the volume of the solvent system, and M is the dipole moment of the solvent system.

DFT calculations were performed using Q-Chem 4.2 (52) to estimate pK_a values and compute binding energies (details in *SI Appendix*, Tables S4–S7). The pK_a values were calculated using a thermodynamic cycle approach (*SI Appendix*, Fig. S14). The binding enthalpy of Ace-PIP with a range of anions (i.e., ClO₄[−], ClO₃[−], NO₃[−], F[−], Cl[−], Br[−], I[−], and BO₂[−]) was computed as

$$\Delta H_{\text{binding}} = H_{\text{complex}} - H_{\text{Ace-PIP}} - H_{\text{ion}}, \quad [5]$$

where the H refers to the zero-point vibrational energy-corrected electronic energy (*SI Appendix*, Table S8). The isolated Ace-PIP, anion, and anion–Ace-PIP complex were each geometry-optimized in implicit water solvent.

Characterization of NF Performance. A custom three-cell bench-scale filtration system operating in cross-flow mode with a flat sheet membrane cell was used for salt rejection and water permeability tests (details in *SI Appendix*). Observed salt rejection (R_{obs}) was determined by comparing the salt concentration in the feed (C_f) and permeate (C_p) solutions (i.e., $R_{\text{obs}} = 1 - C_p/C_f$). Salt separation experiments were evaluated separately with 2 mM and 20 mM feed solutions of sodium chloride (NaCl). Feed solution pH was monitored and adjusted between 3.5 and 10.5 with sodium hydroxide (NaOH) and sulfuric acid (H₂SO₄). Feed and permeate samples were collected for anion analysis, where ion chromatography was used to measure anion concentrations with a Dionex DX-500 ion chromatograph equipped with an AS14A IonPac column.

Data Availability. Raw images and tabulated measurement data have been deposited in Zenodo (<https://zenodo.org/record/3974975#.X5HHce1OIPY>).

ACKNOWLEDGMENTS. This work was supported as part of the Center for Enhanced Nanofluidic Transport, an Energy Frontier Research Center funded by the US Department of Energy, Office of Science, Basic Energy Sciences under Award DE-SC0019112. We also acknowledge the NSF Graduate Research Fellowship awarded to C.L.R.

1. M. Elimelech, W. A. Phillip, The future of seawater desalination: Energy, technology, and the environment. *Science* **333**, 712–717 (2011).
2. J. R. Werber, C. O. Osuji, M. Elimelech, Materials for next-generation desalination and water purification membranes. *Nat. Rev. Mater.* **1**, 16018 (2016).
3. M. Pontie, J. S. Derauw, S. Plantier, L. Edouard, L. Bailly, Seawater desalination: Nanofiltration—A substitute for reverse osmosis? *Desalination Water Treat.* **51**, 485–494 (2013).
4. D. Chen, J. R. Werber, X. Zhao, M. Elimelech, A facile method to quantify the carboxyl group areal density in the active layer of polyamide thin-film composite membranes. *J. Membr. Sci.* **534**, 100–108 (2017).

5. O. Coronell, B. J. Mariñas, X. Zhang, D. G. Cahill, Quantification of functional groups and modeling of their ionization behavior in the active layer of FT30 reverse osmosis membrane. *Environ. Sci. Technol.* **42**, 5260–5266 (2008).
6. V. Freger, Nanoscale heterogeneity of polyamide membranes formed by interfacial polymerization. *Langmuir* **19**, 4791–4797 (2003).
7. A. Szymczyk, P. Fievet, Investigating transport properties of nanofiltration membranes by means of a steric, electric and dielectric exclusion model. *J. Membr. Sci.* **252**, 77–88 (2005).
8. Y. S. Oren, P. M. Biesheuvel, Theory of ion and water transport in reverse-osmosis membranes. *Phys. Rev. Appl.* **9**, 024034 (2018).

9. A. S. Al-Amoudi, Factors affecting natural organic matter (NOM) and scaling fouling in NF membranes: A review. *Desalination* **259**, 1–10 (2010).
10. T. Tong, S. Zhao, C. Boo, S. M. Hashmi, M. Elimelech, Relating silica scaling in reverse osmosis to membrane surface properties. *Environ. Sci. Technol.* **51**, 4396–4406 (2017).
11. W. R. Bowen, J. S. Welfoot, Modelling the performance of membrane nanofiltration – critical assessment and model development. *Chem. Eng. Sci.* **57**, 1121–1137 (2002).
12. H. F. Ridgway, J. Orbell, S. Gray, Molecular simulations of polyamide membrane materials used in desalination and water reuse applications: Recent developments and future prospects. *J. Membr. Sci.* **524**, 436–448 (2017).
13. O. Coronell, M. I. González, B. J. Mariñas, D. G. Cahill, Ionization behavior, stoichiometry of association, and accessibility of functional groups in the active layers of reverse osmosis and nanofiltration membranes. *Environ. Sci. Technol.* **44**, 6808–6814 (2010).
14. O. Coronell, B. J. Mariñas, D. G. Cahill, Accessibility and ion exchange stoichiometry of ionized carboxylic groups in the active layer of FT30 reverse osmosis membrane. *Environ. Sci. Technol.* **43**, 5042–5048 (2009).
15. O. Coronell, B. J. Mariñas, D. G. Cahill, Depth heterogeneity of fully aromatic polyamide active layers in reverse osmosis and nanofiltration membranes. *Environ. Sci. Technol.* **45**, 4513–4520 (2011).
16. W. Choi et al., Thin film composite reverse osmosis membranes prepared via layered interfacial polymerization. *J. Membr. Sci.* **527**, 121–128 (2017).
17. F. A. Pacheco, I. Pinnau, M. Reinhard, J. O. Leckie, Characterization of isolated polyamide thin films of RO and NF membranes using novel TEM techniques. *J. Membr. Sci.* **358**, 51–59 (2010).
18. Q. F. Zhang et al., Novel insights into the interplay between support and active layer in the thin film composite polyamide membranes. *J. Membr. Sci.* **537**, 372–383 (2017).
19. G. M. Geise, D. R. Paul, B. D. Freeman, Fundamental water and salt transport properties of polymeric materials. *Prog. Polym. Sci.* **39**, 1–42 (2014).
20. Z. Jiang, S. Karan, A. G. Livingston, Water transport through ultrathin polyamide nanofilms used for reverse osmosis. *Adv. Mater.* **30**, 1705973 (2018).
21. A. E. Childress, M. Elimelech, Relating nanofiltration membrane performance to membrane charge (electrokinetic) characteristics. *Environ. Sci. Technol.* **34**, 3710–3716 (2000).
22. S. D. Jons, K. J. Stutts, M. S. Ferritto, W. E. Mickols, “Treatment of composite polyamide membranes to improve performance.” US Patent 5,876,602 (1999).
23. F. Helfferich, *Ion Exchange* (McGraw-Hill Book Company, Inc., New York, 1962).
24. S. A. Miller, E. Kim, D. H. Gray, D. L. Gin, Heterogeneous catalysis with cross-linked lyotropic liquid crystal assemblies: Organic analogues to zeolites and mesoporous sieves. *Angew. Chem. Int. Ed. Engl.* **38**, 3021–3026 (1999).
25. W. Guan, S. X. Li, M. A. Reed, Voltage gated ion and molecule transport in engineered nanochannels: Theory, fabrication and applications. *Nanotechnology* **25**, 122001 (2014).
26. A. E. Yaroshchuk, Dielectric exclusion of ions from membranes. *Adv. Colloid Interface Sci.* **85**, 193–230 (2000).
27. Y. Marcus, *Ions in Solution and their Solvation* (John Wiley & Sons, Inc., Hoboken, NJ, 2015).
28. A. Efligenir, P. Fievet, S. Deon, R. Salut, Characterization of the isolated active layer of a NF membrane by electrochemical impedance spectroscopy. *J. Membr. Sci.* **477**, 172–182 (2015).
29. L. Fumagalli et al., Anomalous low dielectric constant of confined water. *Science* **360**, 1339–1342 (2018).
30. R. Nap, P. Gong, I. Szleifer, Weak polyelectrolytes tethered to surfaces: Effect of geometry, acid-base equilibrium and electrical permittivity. *J. Polymer Sci. B Polymer Phys.* **44**, 2638–2662 (2006).
31. E. L. Mehler, G. Eichele, Electrostatic effects in water-accessible regions of proteins. *Biochemistry* **23**, 3887–3891 (1984).
32. K. Kosutic, L. Kastelan-Kunst, B. Kunst, Porosity of some commercial reverse osmosis and nanofiltration polyamide thin-film composite membranes. *J. Membr. Sci.* **168**, 101–108 (2000).
33. N. Fridman-Bishop, V. Freger, When salt-rejecting polymers meet protons: An electrochemical impedance spectroscopy investigation. *Langmuir* **33**, 1391–1397 (2017).
34. N. Fridman-Bishop, V. Freger, What makes aromatic polyamide membranes superior: New insights into ion transport and membrane structure. *J. Membr. Sci.* **540**, 120–128 (2017).
35. M. Stolov, V. Freger, Membrane charge weakly affects ion transport in reverse osmosis. *Environ. Sci. Technol. Lett.* **7**, 440–445 (2020).
36. V. Freger, Kinetics of film formation by interfacial polycondensation. *Langmuir* **21**, 1884–1894 (2005).
37. G. M. Geise, H. B. Park, A. C. Sagle, B. D. Freeman, J. E. McGrath, Water permeability and water/salt selectivity tradeoff in polymers for desalination. *J. Membr. Sci.* **369**, 130–138 (2011).
38. V. Freger, Swelling and morphology of the skin layer of polyamide composite membranes: An atomic force microscopy study. *Environ. Sci. Technol.* **38**, 3168–3175 (2004).
39. E. P. Chan, A. P. Young, J. H. Lee, J. Y. Chung, C. M. Stafford, Swelling of ultrathin crosslinked polyamide water desalination membranes. *J. Polymer Sci. B Polymer Phys.* **51**, 385–391 (2013).
40. J. Q. Luo, Y. H. Wan, Effects of pH and salt on nanofiltration—A critical review. *J. Membr. Sci.* **438**, 18–28 (2013).
41. R. Epsztein, E. Shaulsky, N. Dizge, D. M. Warsinger, M. Elimelech, Role of ionic charge density in donnan exclusion of monovalent anions by nanofiltration. *Environ. Sci. Technol.* **52**, 4108–4116 (2018).
42. M. Bauman, A. Kosak, A. Lobnik, I. Petrinic, T. Luxbacher, Nanofiltration membranes modified with alkoxysilanes: Surface characterization using zeta-potential. *Colloids Surf. A Physicochem. Eng. Asp.* **422**, 110–117 (2013).
43. J. M. S. Henis, M. K. Tripodi, Composite hollow fiber membranes for gas separation – the resistance model approach. *J. Membr. Sci.* **8**, 233–246 (1981).
44. S. Bason, V. Freger, Phenomenological analysis of transport of mono- and divalent ions in nanofiltration. *J. Membr. Sci.* **360**, 389–396 (2010).
45. V. Freger, Ion partitioning and permeation in charged low-T* membranes. *Adv. Colloid Interface Sci.* **277**, 102107 (2020).
46. G. M. Geise et al., Water purification by membranes: The role of polymer science. *J. Polymer Sci. B Polymer Phys.* **48**, 1685–1718 (2010).
47. D. H. Wu, Y. F. Huang, S. C. Yu, D. Lawless, X. S. Feng, Thin film composite nanofiltration membranes assembled layer-by-layer via interfacial polymerization from polyethylenimine and trimesoyl chloride. *J. Membr. Sci.* **472**, 141–153 (2014).
48. C. Boo et al., High performance nanofiltration membrane for effective removal of perfluoroalkyl substances at high water recovery. *Environ. Sci. Technol.* **52**, 7279–7288 (2018).
49. S. L. Walker, S. Bhattacharjee, E. M. V. Hoek, M. Elimelech, A novel asymmetric clamping cell for measuring streaming potential of flat surfaces. *Langmuir* **18**, 2193–2198 (2002).
50. S. Plimpton, Fast parallel algorithms for short-range molecular-dynamics. *J. Comput. Phys.* **117**, 1–19 (1995).
51. M. T. Humbert, Y. Zhang, E. J. Maginn, PyLAT: Python LAMMPS analysis tools. *J. Chem. Inf. Model.* **59**, 1301–1305 (2019).
52. Y. H. Shao et al., Advances in molecular quantum chemistry contained in the Q-Chem 4 program package. *Mol. Phys.* **113**, 184–215 (2015).